FEATURE ARTICLE

Mesoscopic Metal Particles and Wires by Electrodeposition

Reginald M. Penner*

Department of Chemistry, University of California, Irvine, Irvine, California 92679-2025

Received: August 18, 2001; In Final Form: December 12, 2001

The electrodeposition of metal onto a low energy electrode surface like graphite or H-terminated silicon produces mesoscopic metal particles that are broadly distributed in diameter. Broad size distributions are observed even in cases where the nucleation of metal is temporally controlled. For this reason, electrodeposition has been infrequently used as a means for obtaining metal nanostuctures. The central problem is the diffusional "cross-talk" that exists between neighboring metal nanostructures on the electrode surface. Evidence for this diffusional interparticle coupling is encoded into particle size and position distributions obtained from experimental data and from Brownian Dynamics computer simulations of nanostructure growth. Diffusional cross-talk between nanostructures can be turned off using either of two growth strategies described in this paper. These methods permit the size-selective electrodeposition of metal nanoparticles and nanowires that are narrowly distributed in diameter.

I. Introduction

Mesoscopic[1] metal structures play a central role in the emerging area of nanotechnology, and tremendous resources are being devoted to the development of new methods for preparing nanometer and micron scale metal particles, wires, and more complex topologies. One of the most successful strategies for preparing metal nanoparticles[2−24] and, more recently, metal nanorods[25−27] has been solution-phase chemical or photochemical synthetic methods.

This paper is about preparing mesoscopic metal particles and wires by electrodeposition onto graphite electrodes (specifically, highly oriented pyrolytic graphite or HOPG). Superficially, at least, the electrodeposition of metal nanostructures at HOPG is similar to the precipitation from solution of colloidal metal particles because metals interact very weakly with the coordinately saturated graphite basal plane surface. Two differences are that the graphite surface assumes the role of the solution-phase reductant such as citrate[6] and the precipitated metal particles remain in weak van der Waals contact with the surface. Colloid chemists are able to produce suspensions of metal nanoparticles and rods with a high degree of size monodispersity (RSD_{dia}[28] < 10%).[18,21] The most generally useful method for obtaining narrow size distributions in chemical synthesis involves a strategy described by LaMer more than 50 years ago.[29] When this same strategy is implemented to grow metal nanoparticles on an electrode surface, it fails.[30,31] In fact, no strategy has worked very well: The electrodeposition of a metal onto an electrode surface (metal, carbon, or semiconductor) can be carried out under conditions where a smooth electrodeposit is obtained, but until recently, metal particles, wires, and other topologies have not been prepared with any degree of dimensional control.

There are several important exceptions to this broad generalization. Electrodeposition provides a versatile method for producing metal nanoparticles and nanowires in the pores of polycarbonate, mica, and aluminum oxide templates.[32−53] In this case, the template imparts size control. Behm et al.[54−57] have obtained periodic arrays of size-similar metal islands by electrochemically decorating defects on the reconstructed gold-(111) surface. Kolb et al.[58−64] have transferred electrodeposited metal from the tip of an atomic force microscope to a metal surface. Metal nanoparticles that are narrowly dispersed in size are thereby obtained. For example, hundreds of copper nanoparticles have been positioned in a square array on a gold surface using this approach. Finally, electrodeposition has proven to be a powerful method for producing both ultrathin magnetic films[65,66] and magnetic multilayers.[67−71] Individual magnetic layers in these films are tens of nanometers in thickness or less.

These are the exceptions that prove the rule. In general, the electrodeposition of metal on an electrode proceeds according to either of two mechanisms: At high energy surfaces (e.g., noble metals), layer-by-layer deposition occurs initially and is succeeded by three-dimensional growth and coarsening of the metal deposit.[72] This layer-by-layer growth mode is exploited to prepare magnetic multilayers. At low energy surfaces (e.g., H-terminated silicon and graphite), metal particles are promptly formed and the size distribution of these particles becomes monotonically broader during the deposition.[48,73] There has been no general way to electrodeposit millions or billions of mesoscopic metal structures (particles, wires, etc.) that are narrowly dispersed in size.

A few years ago my research group began to ask, "What is the obstacle to the electrodeposition of dimensionally uniform mesoscopic structures?" and, when the answer to this question became apparent, "How can this obstacle be overcome?" In this paper, I summarize the work of my research group in this direction.

* To whom correspondence should be addressed. E-mail: rmpenner@uci.edu.
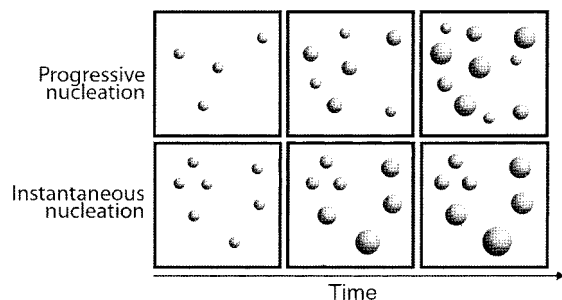
II. Following, Unsuccessfully, the Lead of Colloid Chemists

A strategy for preparing colloid particles that are narrowly dispersed in diameter was formulated by LaMer more than 50 years ago (cf. 29). An oversimplified version of this strategy has two components:[18,21] First, separate the nucleation of particles from the growth of these particles in time. Second, grow these particles from solution phase precursors under conditions of diffusion control. The rational for these requirements can be understood as follows: If the nucleation of new particles occurs "progressively" during growth as shown in Scheme 1 (top), the growth durations for individual particles will be distributed in time and a broad size distribution will be obtained. Ideally, nucleation occurs "instantaneously", that is, for a time interval that is short relative to the duration of particle growth. In this case (Scheme 1, bottom), the growth duration for every particle on the surface is equal, or nearly so. Achieving the needed degree of temporal control over nucleation generally poses the biggest barrier to particle size control for the preparation of size-monodisperse aerosols and colloids, and a variety of innovative solutions to the problem have been developed.[18,21]

The argument for diffusion-controlled growth, articulated in a classic paper by Reiss,[74] relates to the particle growth law. If the particle growth reaction occurs under conditions of kinetic control, the reaction rate at each particle will be proportional to its surface area, and the particle growth law is[75]

$$r(t) = kV_{m}C^{*}t \qquad (1)$$

where k is the rate constant for the particle growth reaction (cm s^{-1}), V_{m} is the molar volume of the metal, and C^{*} is the bulk concentration of metal. Because the time derivative of eq 1 is a constant, the particle size distribution existing at the end of nucleation is preserved during growth. A particle growth reaction that is rapid enough to deplete reactant at the particle surface leads instead to diffusion-controlled growth, and the growth law

$$r(t) = \sqrt{2V_{m}DC^{*}t} \qquad (2)$$

where D is the diffusion coefficient for metal ions. For eq 2, $dr/dt \propto t^{-1/2}$ and the distribution of particles formed by nucleation becomes narrower during growth as small members of this distribution catch up with large members of the distribution. Equation 2 applies both to spherical colloid particles growing in solution and to hemispherical particles that are confined during growth to a flat electrode surface. In colloid syntheses where both instantaneous nucleation and diffusion-controlled growth are achieved, extremely narrow particle size
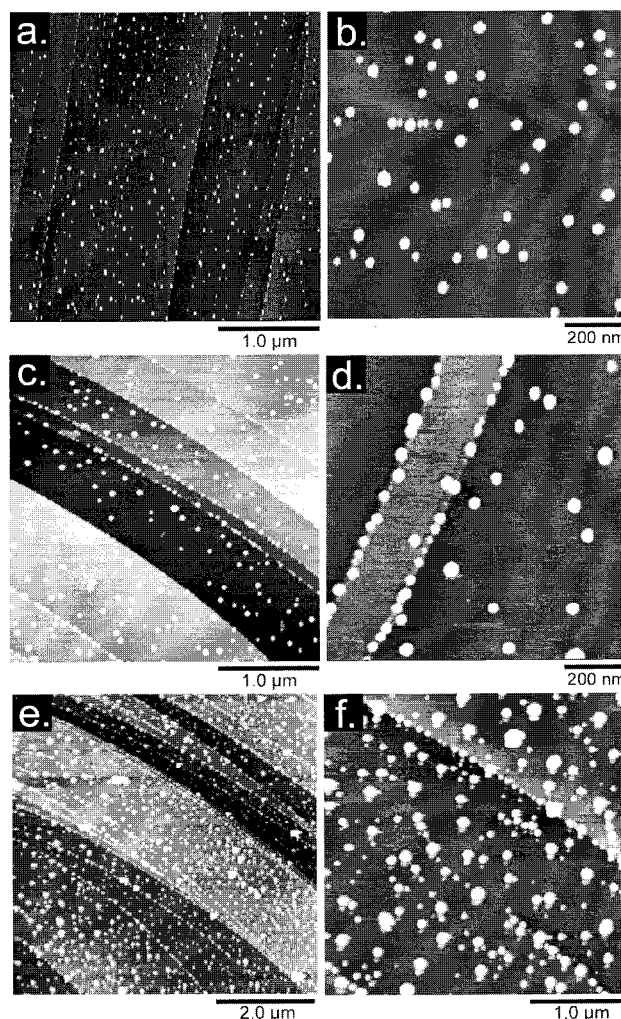

Figure 1. Noncontact atomic force microscope (NC-AFM) images of the graphite basal plane surface following the electrodeposition of platinum nanoparticles from aqueous 1.0 mM PtCl$_6$$^{2-}$, 0.10 M HCl using an overpotential of -500 mV vs MSE. (a and b) The deposition duration, $t_{dep} = 10$ ms, which yielded 0.02 equivalent platinum atomic layers. The mean particle diameter, $\langle dia \rangle$, on this surface was 2.5 $\pm$ 0.9 nm; (c and d) $t_{dep} = 50$ ms, 0.15 equiv atomic layers, $\langle dia \rangle = 5.4 \pm 1.3$ nm; (e and f) $t_{dep} = 100$ ms, 0.32 equiv atomic layers, $\langle dia \rangle = 7.2 \pm 3$ nm.

distributions characterized by RSD$_{dia}$ < 10% have been obtained for a wide variety of materials including metals.[6,15,18,21]

We have demonstrated that the electrodeposition of metal particles can also be carried out under conditions of instantaneous nucleation and diffusion-controlled growth at graphite electrode surfaces.[30,31] At a graphite electrode immersed in a metal plating solution, the application of a sufficiently negative voltage to the electrode causes the reduction of metal ions to metal atoms. These metal atoms cluster to form nanoscopic metal particles. Metal clusters form in preference to a metal monolayer because the graphite surface is coordinately saturated and possesses an extremely low interfacial energy.[76] This Volmer−Weber (V−W) mode of growth has been known to surface scientists for many years,[77] but the first clear instance of V−W growth in electrodeposition was reported by Zoval et al. in 1996.[31] In these and subsequent experiments, three-dimensional metal particles were observed using atomic force microscopy (AFM) even after the electrodeposition of less than an atomic layer of metal. Figure 1 parts a and b, for example, shows AFM images of a graphite surface on which the equivalent of just 0.020 atomic layers of platinum were electro-
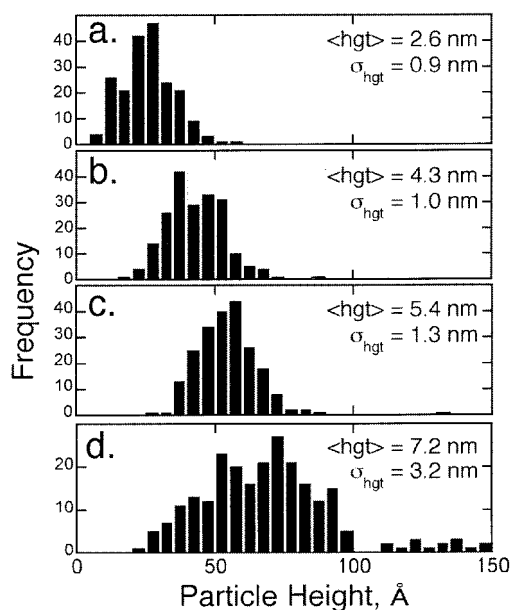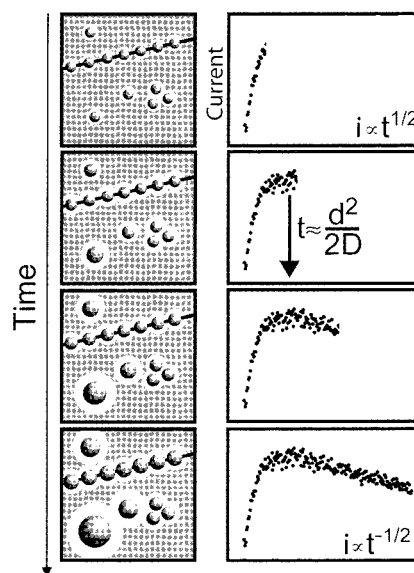
Feature Article

J. Phys. Chem. B, Vol. 106, No. 13, 2002 **3341**

Figure 2. Platinum particle size histograms compiled from NC-AFM image data. Deposition durations were (a) 10, (b) 50, (c) 70, and (d) 100 ms.

SCHEME 2: Evolution of Particle Size Dispersion in Parallel with the Deposition Current

deposited using a 10 ms plating pulse.[30] The bright spots in these AFM images are three-dimensional platinum particles having a mean height of 2.6 nm (the widths of these particles appears much larger in these AFM images because the particle width, but not its height, is convoluted with the tip width during image acquisition). Such data, acquired also for other metals including silver,[31] copper,[78] cadmium,[79,80] and zinc,[81] provided clear evidence for a V−W mechanism of metal deposition at graphite surfaces. For all of these metals, electrodeposition from a 1.0 mM plating solution of M^{n+} (e.g., Ag^+, $PtCl_6^{2-}$, Cd^{2+}, etc.) using $\eta > |-400 \text{ mV}|$ was diffusion-controlled, and metal nanoparticles were produced at a coverage of $5 \times 10^8 - 5 \times 10^9$ cm^{-2}.

As 1−3 nm diameter metal particles were grown for 20−100 ms to 50 nm or more in diameter, the nucleation density measured by AFM remained approximately constant. In the case of platinum, for example, AFM images of surfaces after the deposition of 5.0 nm particles using a 50 ms pulse (Figs. 1c and 1d) and 7.2 nm particles using a 100 ms pulse showed essentially the same number density of particles (($2-3) \times 10^9$ cm^{-2}) as seen in Figure 1 parts a and b. This means that new metal nanoparticles are no longer forming after 10 ms and nucleation is instantaneous. Independent verification of this fact was provided by AFM measurements of the mean particle diameter versus the deposition charge which were consistent with the growth of a fixed number of particles (i.e., the mean particle diameter is proportional to $Q^{1/3}$).[30] Thus, the two requirements for the formation of dimensionally uniform metal particles, instantaneous nucleation and diffusion-controlled growth, were both satisfied for the electrodeposition of metal particles on graphite surfaces. Despite this fact, dimensionally uniform metal particles were not obtained (Scheme 1, bottom). For example, as shown in Figure 2, the 7.2 nm diameter platinum particles produced using a 100 ms voltage pulse (Figure 1 parts e and f) exhibited a standard deviation of 3.2 nm (an RSD$_{dia}$ of nearly 50%). In fact, we have found that for a variety of metals both σ_{dia} and RSD$_{dia}$ increase as a function of the particle diameter and RSD$_{dia}$ > 50% are seen for dispersions of metal nanoparticles with diameters greater than 7−8 nm (Figure 2). The question is "why".

III. Understanding Size Distribution in Electrodeposition

Two factors operating in concert cause the particle size distribution to broaden during the electrodeposition of metal nanoparticles. First, on graphite surfaces the distribution of metal nuclei is "pseudo-random". Nucleation is spatially random on terraces, and nuclei are also aligned at step edges on the surface. Thus "strings" of platinum nuclei at steps are interspersed with randomly nucleated particles on terraces in the AFM images of Figure 1. Second, the growth law for individual metal particles on the surface depends on the number and proximity of neighboring particles. As shown in Scheme 2 (left), the "communication" of a metal particle with its neighbors is mediated by the depletion layer surrounding each particle. Under conditions of diffusion control, this layer of solution that is depleted of metal ions relative to bulk solution extends for 10 particle radii from the surface of each particle. Two particles with overlapping depletion layers both grow more slowly than predicted by eq 2. The distribution of nearest neighbor distances resulting from the randomness of nucleation coupled with a growth law that depends on the number and proximity of other particles on the surfaces leads to a dispersion in the growth rates of individual particles on the surface. In fact, this "interparticle diffusion coupling" or "IDC" is the single most important mechanism of distribution broadening for the growth of randomly nucleated metal particles on electrode surfaces. IDC also exists for colloidal metal particles growing in suspension, but an important difference exists. Whereas an encounter between two growing colloidal particles may retard the growth of each for a brief period, these two particles do not persist in proximity to one another as is the case for two particles that have nucleated close to one another on a graphite surface. The *time-averaged* growth law for all colloidal particles growing at diffusion control can be the same (albeit somewhat slower than predicted by eq 2), whereas this is not so for randomly nucleated particles on an electrode surface.

Three facts implicate IDC as the culprit in electrochemical particle growth experiments: (1) For ensembles of metal particles grown at diffusion control, the diameter of a metal particle is correlated with its proximity to other particles on the electrode surface. These particle size correlations are the "fingerprint" of IDC. (2) Distributions of particles grown in

Brownian Dynamics computer simulations undergo broadening in much the same way as seen experimentally. In these simulations, it can be demonstrated that IDC is the dominant promoter of particle size dispersion. (3) the implementation of experimental strategies designed to eliminate IDC produce a dramatic improvement in the size uniformity of metal particles. We discuss the first of these in section III below. Strategies for defeating IDC are discussed in sections IV−V. We have used Brownian Dynamics computer simulations of metal particle growth to reveal some of the subtleties of IDC. We summarize the results of these simulations next.

Brownian Dynamics computer simulations provide a convenient means for separating the physics of electrochemical particle growth, including IDC, from the chemistry of the metal being deposited. In these simulations, a small area (typically 10^{-9} cm^{-2}) of the graphite surface and the solution adjacent to it is modeled in three dimensions.[82,83] Within the simulated volume, each metal particle and each metal ion in the solution are explicitly modeled as a function of time. An algorithm that simulates Brownian motion generates the motion of each ion; the diffusion coefficient for these ions is adjusted to match the metal ion of interest (e.g., 1.35×10^{-5} cm^2 s^{-1} for Ag$^+$ in aqueous solution). The number and positions of nuclei on the electrode surface are fixed at the beginning of the simulation so that these simulations model the case of instantaneous nucleation. These nascent metal particles begin as single metal atoms and grow to a mean diameter of ∼3 nm from a 10^{-3} M "solution" of metal ions in a 0.5 ms simulation.

Typical plots of the deposition current and the standard deviation of the particle diameter are shown for six experiments in Figure 3.[82] Several features of these simulated data are worth noting. First, the reaction rate (or current) is peaked as a function of the deposition time. For N silver particles growing in isolation, the current is predicted to increase in proportion to $t^{1/2}$:[84]

$$i(t) = \pi F N (2 D_{\mathrm{Ag}^+} C^*_{\mathrm{Ag}^+})^{3/2} (V_{\mathrm{m,Ag}} t)^{1/2} \qquad (3)$$

In eq 3, D_{Ag^+} is the diffusion coefficient for Ag$^+$, C^* is its bulk concentration (10^{-6} mols cm^{-3} for Figure 3), $V_{\mathrm{m,Ag}}$ is the molar volume of silver (10.27 cm^3 mol^{-1}), and F is the Faraday (96 485 C eq^{-1}). As shown schematically in Scheme 2, the current peak seen (at $t = t_c$) in all of the simulations of Figure 3 marks the point of departure for the current transient from the prediction of eq 3. The decrease in current at t_c is caused by IDC. At times $t > t_c$, depletion layers at adjacent particles merge and a planar diffusion layer blankets the entire geometric surface area of the electrode. The current in this "coupled" time regime is exactly the same as that at a planar electrode having the same geometric area, A, and is given by the familiar Cottrell equation:[85]

$$i(t) = \frac{n F A D_{\mathrm{Ag}^+}^{1/2} C^*_{\mathrm{Ag}^+}}{(\pi t)^{1/2}} \qquad (4)$$

So, as N increases, the current transient approximates to a greater and greater extent the current transient seen at a planar electrode surface. Figure 3 also shows that the current transients for particles arranged in a hexagonal array are very similar to those for randomly positioned particles provided the nucleation density is the same.

Also plotted in Figure 3 is the standard deviation of the particle radius, σ_r, as a function of deposition time. At short times ($t < t_c$), the behavior of these σ_r vs time "transients" is
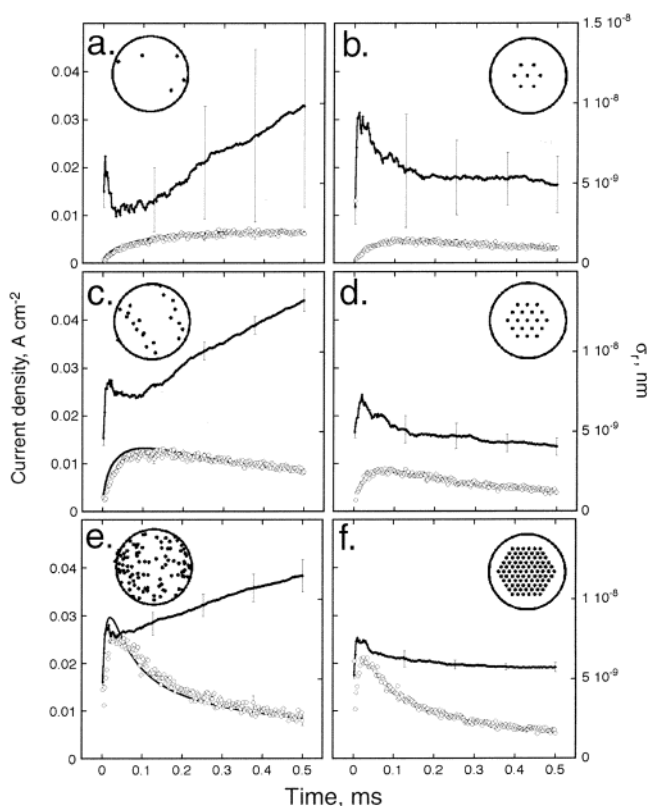

Figure 3. Current density (open circles) and the standard deviation of the particle radius, σ_R, (solid circles) as a function of time for random particle ensembles (a, c, and d) and hexagonal arrays of particle (b, d, and f) at three nucleation densities. These BD simulation results represent the mean of three simulations, each of which involved a different silver plating solution, and different positions for nuclei on the surface. Insets show electrode positions for one of the three simulations. The standard deviation of the σ_R are indicated by the error bars (±1σ) which are shown at five times. The nuleation densities in these simulations were (a) 5×10^9, (b) 7×10^9, (c) 2×10^{10}, (d) 1.9×10^{10}, (e) 2×10^{11}, and (f) 2.2×10^{11} cm^{-2}.

the same whether metal particles are arranged in a hexagonal array or are randomly distributed on the surface: σ_r first increases rapidly to 0.5−1.0 nm and then decreases with time until $t \sim t_c$. This behavior is the same whether particles are randomly distributed on the surface or are arranged in a hexagonal array. We have shown[82] that stochastic processes that are insensitive to particle ordering on the surface govern the particle size dispersion in this time regime. For $t > t_c$, however, the behavior of hexagonal and random ensembles differs: Particles located in a hexagonal array continue to become more size similar, whereas randomly nucleated metal particles transition from convergent growth to divergent growth. For random particle ensembles, the increase in σ_r with time is approximately linear. In Figure 3a, with $N = 5 \times 10^9$ cm^{-2}, for example, the slope of this increase is 0.10 nm ms^{-1}. If this increase in σ_{dia} is extrapolated to a deposition time of 10 ms, a σ_r of 1.0 nm is predicted. As shown for example in Figure 2a for platinum particle growth, this prediction compares favorably with the experiment. The agreement seen between experiment and simulation suggests that the physics of metal particle growth and IDC in particular, not the chemistry of these metal nanoparticles, is responsible for the distribution broadening seen in our experimentals.[82]

If IDC is responsible for distribution broadening for the random ensembles of Figure 3, the size of a metal particle should be correlated with its proximity to other particles on the surface. As shown in Figure 4, this correlation exists over a range of
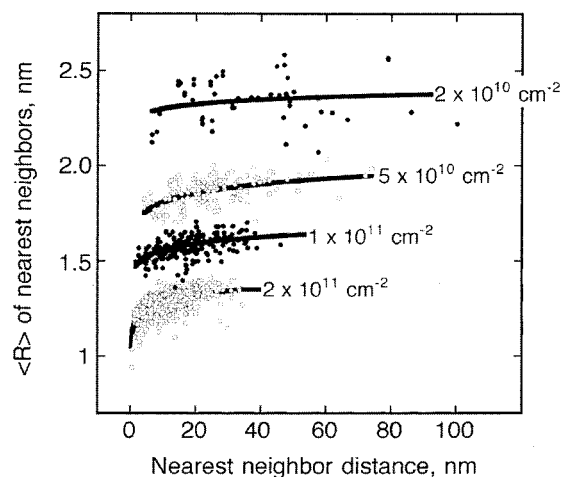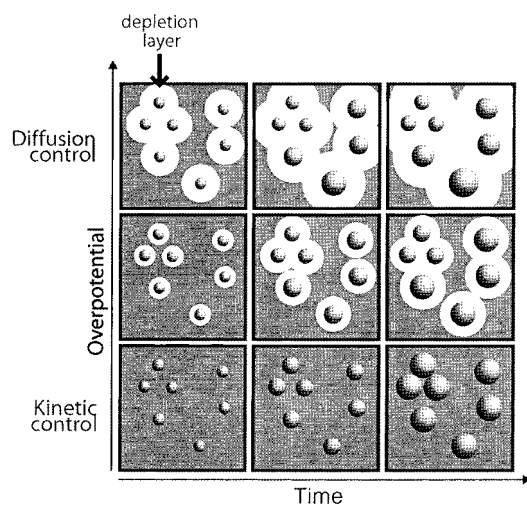
Feature Article

J. Phys. Chem. B, Vol. 106, No. 13, 2002 **3343**

Figure 4. Plots of the mean radius, $\langle R \rangle$, for nearest neighbors as a function of the nearest neighbor distance for four random ensembles. Solid lines represent the least-squares fit of an equation of the form $y = ax^b + c$ to each data set. Each data set is labeled with the nucleation density.

SCHEME 3: Effect of Overpotential, and Hence the Reaction Rate, on the Size Dispersions of Metal Particles as a Function of the Deposition Time

nucleation densities and, as expected, the strength of the correlation is greatest for the highest nucleation densities.[82]

IV. Slow Growth

It is clear from Figure 3 that the adverse effects of IDC are eliminated for particles arranged in a hexagonal array. What, if anything, can be done to eliminate IDC for particles that are randomly positioned on an electrode surface? We have discovered two solutions to this problem.

The most general solution involves reducing the rate of growth for metal particles,[86−88] as shown in Scheme 3. Our discovery of "slow growth" coincided with reports from Plieth et al.[89,90] that this technique could be used to produce silver particles having exceptionally narrow size dispersions. Brownian Dynamics simulations can again be used to illustrate the benefits of this approach. The simulations shown in Figure 3 were carried out under conditions of diffusion control[82] which is achieved using a large deposition overpotential of more than $|-200 \text{ mV}|$. As shown in Scheme 3 (top), IDC is most problematic under these conditions because the perturbation of the metal ion concentration near each growing particle is most pronounced.
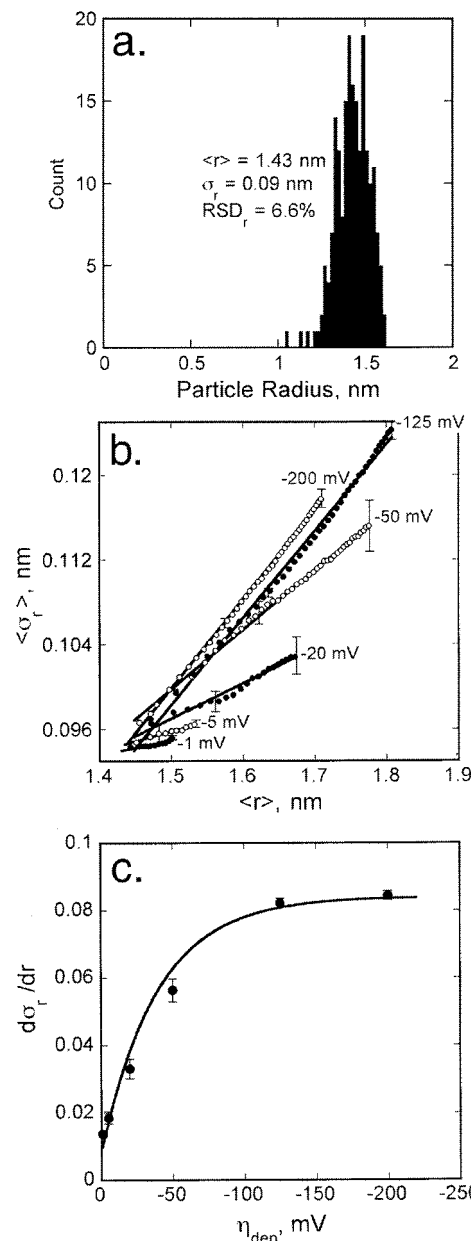

Figure 5. (a) Size distribution for the 200 particle ensemble that served as the starting point for the simulations described in b and c. (b) The standard deviation of the particle radius, σ_r, versus $\langle r \rangle$ for simulations at six overpotentials as indicated. Solid lines are the results of linear least-squares analysis for each overpotential. The error bars in this plot represent $\pm 1\sigma$ for the σ_r obtained from three or four replicate simulations conducted at each overpotential. (c) Plots of the $d\sigma_r/dr$ vs $\langle r \rangle$ for the growth of the distribution shown in a at six overpotentials based on a linear least-squares analysis of the data shown in b. The error bars in this plot represent $\pm 1\sigma$ for $d\sigma_r/dr$ obtained from three or four replicate simulations conducted at each overpotential.

We explored the effect of lower deposition potentials on the dimensional uniformity of metal particles obtained in Brownian Dynamics simulations of particle growth. Starting with the distribution of 200 particles shown in Figure 5a, for example, we used Brownian Dynamics simulations to electrodeposit at overpotentials ranging from −1 mV to −200 mV. As the overpotential was reduced down to −1 mV, $d\sigma_r/\langle r \rangle$ decreased to just an eighth of its value at −200 mV (Figure 5b,c).[83] At the lowest overpotentials investigated in this study, no evidence for IDC was seen in particle−nearest neighbor correlations.[83] Slow growth is an effective means for eliminating IDC because
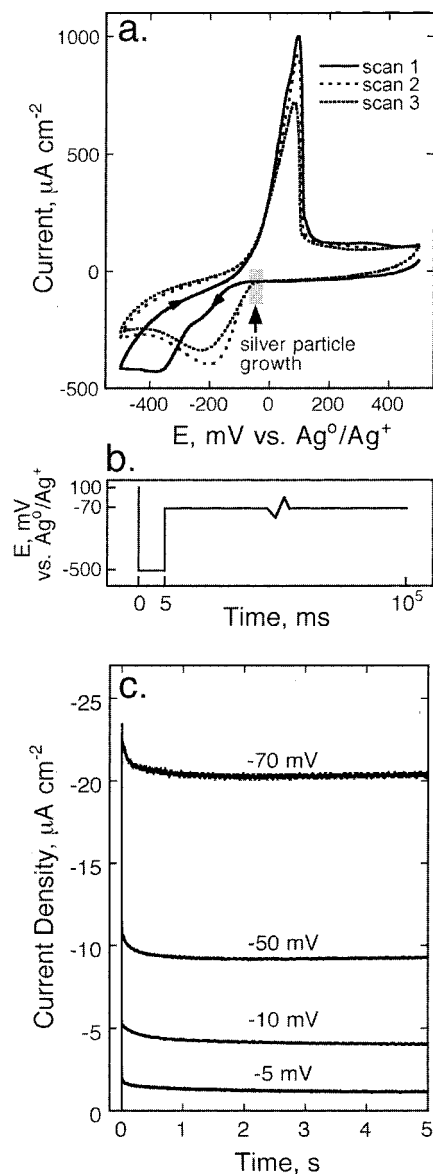
Figure 6. (a) Cyclic voltammograms at 20 mV s^{-1} for a HOPG electrode immersed in a silver plating solution consisting of 1.0 mM AgClO$_4$, 0.1 M LiClO$_4$ in acetonitrile. (b) Schematic of the double plating pulse used to obtain silver particles. (c) Current versus time transients for the electrodeposition of silver on HOPG at specified plating overpotentials as shown.

the radius of the depletion layer adjacent to each particle is reduced as the growth rate is reduced (Scheme 3, bottom).

Experimentally, slow growth is implemented by applying two voltage pulses in rapid succession (Figure 6a,b). The first is a nucleation pulse lasting just 5–10 ms and having an overpotential of ∼−500 mV. This pulse produces ∼1 nm diameter "seed" nanoparticles pseudorandomly on the graphite surface. Immediately following the nucleation pulse, a growth voltage pulse with an overpotential of −50 to −100 mV and lasting up to a minute is applied.[88] As shown in Figure 6a for silver, the potential of this growth pulse is at the foot of the metal plating wave in a cyclic voltammogram acquired at a clean electrode in the metal plating solution. At this potential, the rate of nucleation is exceedingly slow, so in addition to eliminating IDC during particle growth, the double pulse has the added benefit of enforcing a separation between nucleation and growth in time.
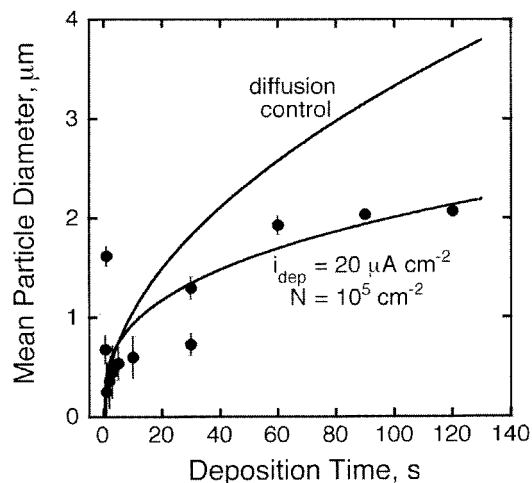

Figure 7. Plot of mean particle diameter, measured by SEM, versus electrodeposition time for silver particle deposition experiments conducted at −70 mV vs Ag$^+$/Ag$^{\circ}$. Solid lines are the predicted diameter versus time for diffusion-controlled deposition, and using eq 5 for deposition carried out at a constant current, i_{dep}, as indicated.

The current observed during growth is virtually constant, as shown again for silver in Figure 6c. The time-invariant flux of the metal ion responsible for this current is supplied by the natural convection present in the electrochemical cell. Because of the time-invariance of the plating current, the growth law for metal particles is given by[87,88]

$$r(t) = \left[\frac{3}{2}\frac{i_{dep}tV_m}{z\pi FN}\right]^{1/3} \qquad (5)$$

where i_{dep} is the plating current. This growth law is seen experimentally, as shown in Figure 7.[88] As originally observed by Bradford et al.,[91] any growth law having $r \propto t^n$ with $n < 1.0$ should cause particle size distributions to become narrower as a function of time. In principle, this is an added and unexpected benefit of the slow growth strategy. In practice, we find that the metal particle distributions produced by slow growth are characterized by a σ_{dia} that is only weakly affected by growth time. As shown in Figure 8b, for example, six separate silver particle dispersions with mean diameters ranging from 240 nm to 2 μm all show σ_{dia} of 80–150 nm. This is an aspect of this experiment that remains under investigation in our laboratory. RSD$_{dia}$ values as low as 6% are seen for micron scale silver particles.[88] This degree of size monodispersity, which compares favorably with state-of-the art colloid synthetic methods, is obtained for relatively large particles with diameters of a micron or so.

Because slow growth affects the physics of particle growth, it should be an effective means for producing size-similar mesoscopic metal particles for any metal that can be electrodeposited. We have surveyed six metals (Pt, Au, Ag, Cu, Ni, and Cd) and one metal oxide (MoO$_2$) to date and found that highly size monodisperse particles are obtainable for each using this approach.[87,88] Typical scanning electron micrographs are shown in Figure 9 (see also Table 1).

V. Nanocrystalline Metal Particles by H$_2$ Coevolution

The second strategy for equalizing the growth rates of metal nanoparticles is to generate convective mixing of the plating solution in the vicinity of each metal particle. The standard method for producing convective mixing at a planar disk-shaped electrode surface is to rotate the electrode about an axis
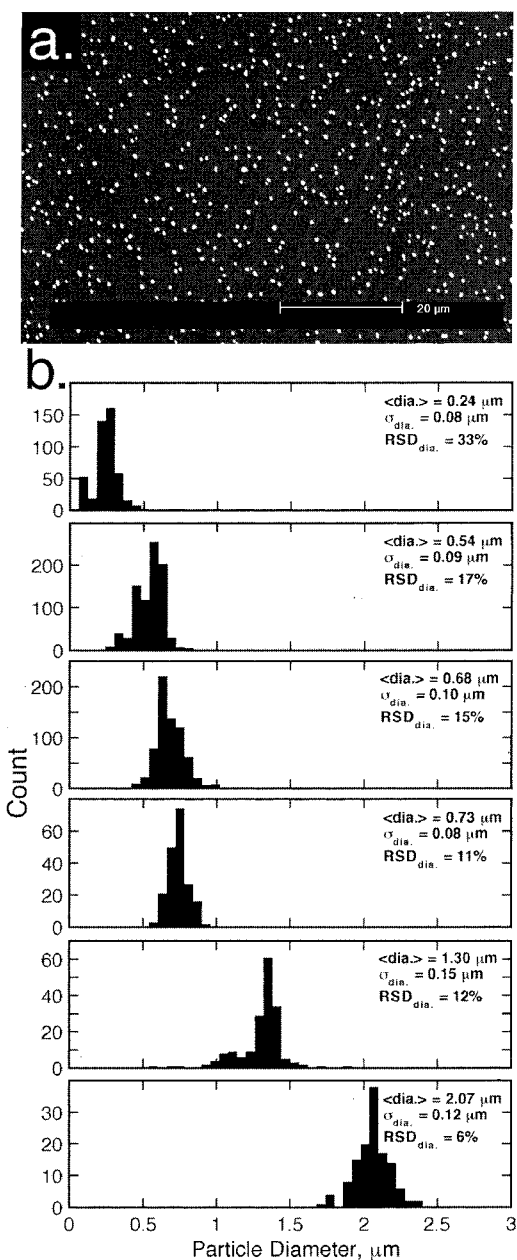
Feature Article

J. Phys. Chem. B, Vol. 106, No. 13, 2002 **3345**

Figure 8. (a) Representative scanning electron micrographs (SEMs) of silver particles prepared using slow growth. (b) Particle size histograms for samples prepared using the plating solution as in Figure 6 using a deposition potential of −70 mV and deposition durations (top to bottom) of 500 ms, 1.0 s, 5.0 s, 10 s, 30 s, and, 120 s.
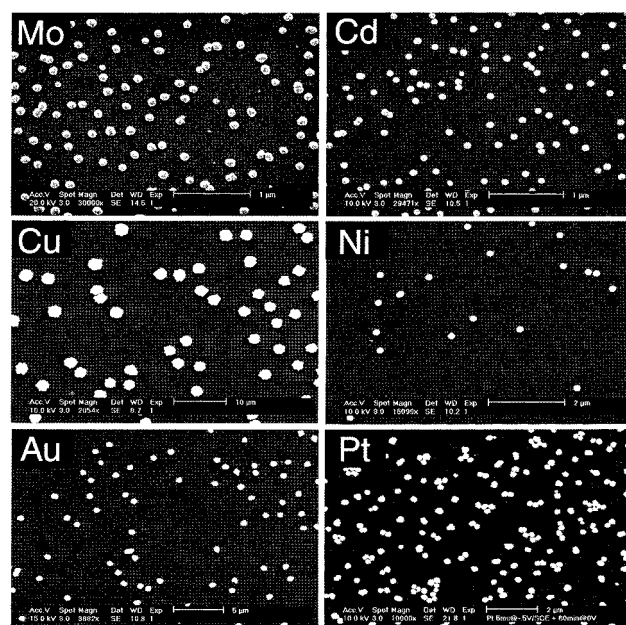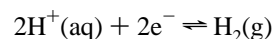

Figure 9. SEMs of metal particles prepared using the slow growth method. Deposition solutions and potentials are as indicated in Table 1. The deposition current density observed in each experiment was as follows: (Mo) 180−140, (Cd) 40−60, (Cu) 40−60, (Ni) 240−260, (Au) 30−40, and (Pt) 5−100 μA cm^{-2}.

s^{-1}, a rotation rate 2 orders of magnitude greater than the maximum for the RDE.[85] This exercise demonstrates the difficulty associated with propagating convective mixing from the bulk of the plating solution to within a micron of the electrode surface.

This problem can be circumvented by locating a source of convection within this thin boundary layer. One way to accomplish this is by driving a second, gas-evolving electrochemical process in parallel with metal electrodeposition. The formation of gas bubbles coupled with the release of these bubbles from the surface and their motion through the electrolyte near the electrode surface produces the required convective mixing. This is an old idea: Foerster recognized the utility of gas evolution for enhancing convective mixing in 1924.[92] More recent studies by Tobias and co-workers[93,94] have produced a quantitative description of the convection generated by gas evolution. For electrodeposition experiments conducted in aqueous solutions, the natural choice for the gas evolving reaction is proton reduction:

$$2H^+(aq) + 2e^- \rightleftharpoons H_2(g)$$

We have used "H$_2$ coevolution" to equalize the growth rates of mesoscale nickel particles on graphite. The logistics of this experiment can be understood with reference to Figure 10. In Figure 10a, a cyclic voltammogram is shown for a graphite electrode in a nickel plating solution containing 10 mM Ni^{2+} with pH = 8.3. In this solution, an onset for nickel electrodeposition and H$_2$ evolution is seen at approximately −1.2V vs MSE,[95] although the voltammetric waves for these two processes are not resolved. Nickel oxidation is seen on the positive-going scan at a potential of −0.8 V.

Current versus time transients for the electrodeposition of nickel from this solution are shown in Figure 10b. As the plating potential is reduced from −1.0 to −1.4 V, the current increases by a factor of 400 as nickel electrodeposition begins to occur. Within this potential interval, little H$_2$ evolution occurs, and

perpendicular to the plane of its surface. For such a "rotating disk electrode" or RDE, the thickness of the hydrodynamic boundary layer adjacent to the electrode surface, y_h, is related to the rotation rate through[85]

$$y_h = 3.6(\nu/\omega)^{1/2} \tag{6}$$

where ν is the kinematic viscosity of the solution ($\sim$0.010 cm^2 s^{-1} for dilute aqueous solutions) and ω is the angular rate of rotation. For efficient stirring to be induced at mesoscale metal particles on an electrode surface, y_h must approach the diameter of these particles, and the required value of ω can be calculated using eq 6. This calculation leads immediately to the conclusion that the RDE will be incapable of producing convection that is effective for equalizing the growth rates of mesoscale metal particles. For example, $y_h = 1.0$ μm requires $\omega = 1.3 \times 10^7$

TABLE 1: Plating Solutions and Potentials Used for the Generation of Mesoscale Metal (or Metal Oxide) Particles Shown in Figure 9

metal	plating solution[a]	rev. potential (V vs SCE)	plating potential(s) (V vs SCE)
platinum	1 mM $PtCl_6^{2-}$, 0.1 M HCl	$\approx +0.30$	+0.15 to −0.03
gold	1 mM $AuCl_3$, 0.1 M NaCl	0.60	0.55
silver	1 mM $AgClO_4$, 0.1 M $LiClO_4$, acetonitrile	0.38	0.24
nickel	0.01 M $Ni(NO_3)_2$, 0.2 M NaCl, 0.2 M NH_4Cl pH = 7.5−8.5	−0.70	−0.80
copper	1 mM $CuSO_4$, 0.1 M K_2SO_4	0.19	0.13
cadmium	10 mM CdF_2, 0.1 M NaF	−0.77	−0.82 to −0.89
molybdenum dioxide	1.0 mM MoO_4^{2-}, 1.0 M NaCl, 1.0 M NH_4Cl, pH = 7.5−8.5	$\approx$-0.60	−0.78

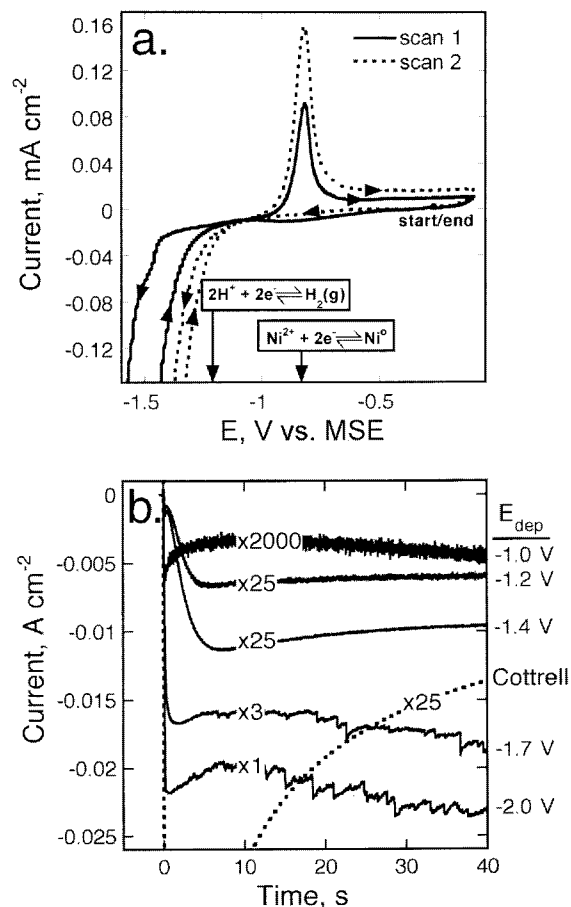[a] All solutions are aqueous unless otherwise indicated.

Figure 10. (a) Cyclic voltammograms for a highly oriented pyrolytic graphite (HOPG) electrode at 20 mV s^{-1} acquired in aqueous 10 mM $Ni(NO_3)_2$, 1 M NaCl, 1 M NH_4Cl, pH = 8.3. (b) Current versus time transients for the electroplating of nickel on freshly cleaved HOPG at various deposition potentials (vs MSE) as indicated.

Figure 11. Photomicrographs of hydrogen evolution at an HOPG electrode immersed in the plating solution indicated in Figure 10. Images a−d were acquired at four times, following the application of a −2.0 V vs MSE plating pulse. The electrode shown here is approximately 1.0 cm in width.

the nickel plating current remains below the Cottrell limit (dashed line) as expected for the diffusion-controlled plating of Ni^{2+}. At more negative potentials, nickel electrodeposition and proton reduction occur concurrently. Current transients acquired at −1.7 and −2.0 V exhibit noise, and the plating current rapidly increases to values above the Cottrell limit.[96] Relative to the experiment at −1.4 V, the extra current seen at more negative potentials has two sources: the onset of proton reduction and the convective transport of Ni^{2+} to the electrode surface caused by hydrogen gas evolution. The noise in the deposition current derives from the formation of hydrogen gas bubbles. The scale of the gas bubbles formed at −2.0 V can be seen in the photographs shown in Figure 11.
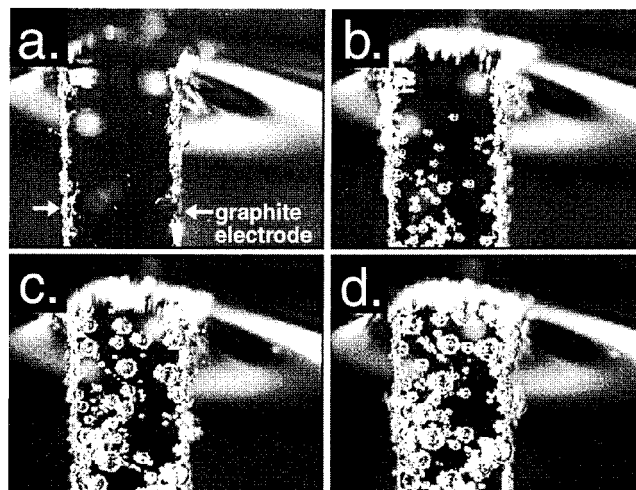
The onset of hydrogen evolution is associated with a narrowing of the particle size distribution for electrodeposited nickel particles. This effect is shown in the scanning electron micrographs of Figure 12, which show graphite surfaces following the electrodeposition of nickel at −1.2, −1.6, and −2.0 V. Nickel particles prepared at −1.2 V were heterogeneous in size with diameters ranging from 10 to more than 250 nm. The RSD$_{dia}$ for this sample was 43%. Particles of approximately the same mean diameter prepared at −1.6 and −2.0 V exhibited better dimensional uniformity characterized by RSD$_{dia}$ of 23 and 14%, respectively.[96] Although we cannot deconvolute the hydrogen evolution current from the nickel electrodeposition current in these experiments, a subjective evaluation of the rate of H$_2$ evolution based on observations of the electrode surface reveals that H$_2$ evolution is absent at −1.2 V, occurs slowly at −1.6 V, and is vigorous at −2.0 V. We conclude that the size distribution narrowing observed at negative plating potentials is associated with the formation of H$_2$ gas bubbles at the electrode surface.

Whereas the metal particles produced by slow growth are single crystalline and highly faceted, those produced by H$_2$ coevolution are unfaceted because they are nanocrystalline. The nanocrystalline structure of these particles is manifested in several ways in the electron microscopy data. First, as shown in Figure 13a, selected area electron diffraction lines have a measurable width. Scherrer analysis[97] of these lines reveals a mean crystallite dimension near 2 nm. High magnification SEM

Feature Article

J. Phys. Chem. B, Vol. 106, No. 13, 2002 **3347**
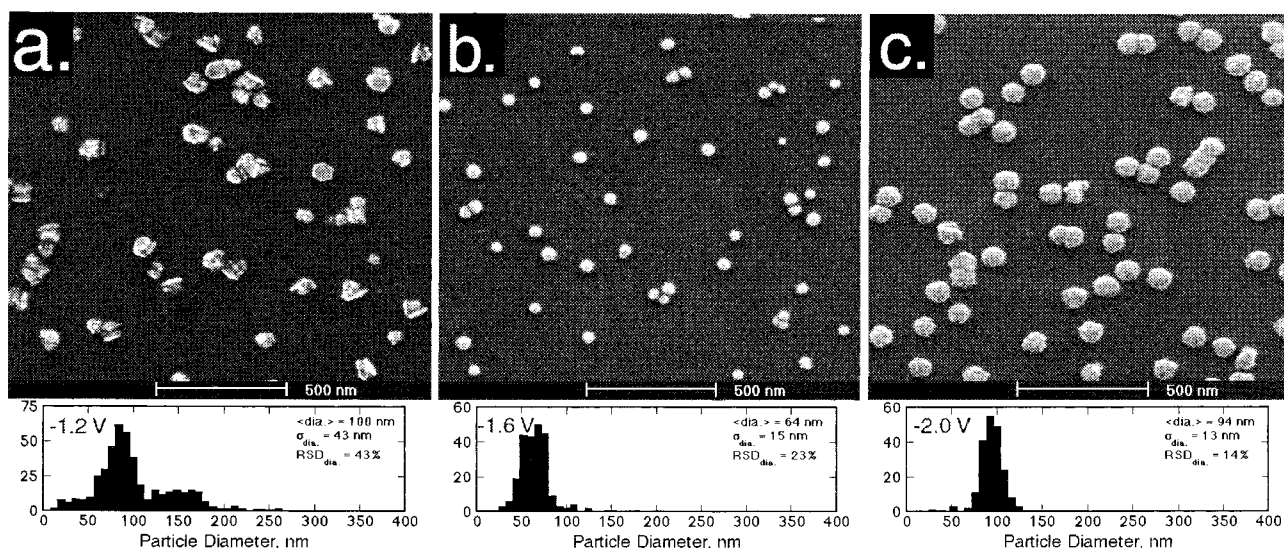

Figure 12. SEM images and particle diameter histograms for nickel particles following electrodeposition at various potentials for various deposition times. The deposition solution is the same as those in the experiments of Figures 10 and 11: (a) −1.2 V vs MSE × 25 min.; (b) −1.6 V × 2.8 s.; (c) −2.0 V × 1.5 s.

images of individual nickel particles reveals that these particles have rough surfaces on this same distance scale. The nanoscopic nickel grains within these particles can be seen in real space in dark field transmission electron microscope images, like that shown in Figure 13c.[96] It is surprisingly difficult to determine the gross shape of these nickel particles from plan-view SEM and TEM images; however, in some SEM images (data not shown), particles that have been upended are seen, and it is clear that these particles are hemispherical in shape with well-defined planar bases.

The detailed mechanism by which these nanocrystalline particles nucleate and grow in a H_2 coevolution experiment is incompletely understood, and we are actively pursuing this mechanism at the moment. In particular, we do not understand how the nanocrystalline structure of these particles is generated during particle growth. It is possible, for example, that 2.0 nm nickel crystallites are formed directly on the graphite electrode surface, are dislodged from the surface by hydrogen bubbles, and are collected onto the larger nickel particles that are eventually observed by SEM. If this mechanism operates, then the magnetic properties of the metal may play an important role in directing the aggregation of nanoscopic grains to form larger particles. To date, H_2 coevolution has been successfully applied to the formation of cobalt and iron particles in addition to nickel, but we have been unsuccessful with silver and other nonferromagnetic metals.

VI. Nanowires

There are few methods for preparing free-standing metal nanowires with diameters below 100 nm and lengths greater than 20 μm. Template synthesis, pioneered by Martin,[33,36−38,40,46,47,51] Moskovits,[32,34,35,49,50,53] Searson,[39,42−45,48,52] and others has been extensively used as a means for preparing metal nanowires that are 2−20 μm in length. Nanowires that are compositionally modulated along their axis are readily prepared using this approach.[42,98] Dai and co-workers[99] have used carbon nanotubes to template the growth by physical vapor deposition of metal nanowires. Because carbon nanotubes can be extremely long, this approach has the potential to yield long metal nanowires in the future. Recently, Murphy and co-workers[25,26] have reported the preparation by solution phase

growth methods of gold and silver nanorods with aspect ratios of 18 or more. Although these nanowires are less than a micron in length, this approach may eventually allow longer metal nanowires to be synthesized in bulk quantities.

We have adapted step edge decoration, an old idea, to the growth by electrodeposition of long metal nanowires on graphite surfaces. In the experiments described above, particle nucleation and growth was either carried out using the same large overpotential of $>|-500$ mV| (as in H_2 coevolution) or metal particles were nucleated using a large amplitude voltage pulse and then grown at a lower overpotential (as in slow growth). Under the influence of a large overpotential, metal nucleation occurs nonselectively and particle growth is observed to occur both on defect-free terraces and at defects such as step edges. However the barrier to metal nucleation is lower at step edges then on terraces, and this energetic disparity can be exploited in an electrodeposition experiment to selectively decorate step edges and produce nanowires.

Step edge decoration is a well-established method for preparing nanowires using physical vapor deposition (PVD) and molecular beam epitaxy (MBE). Himpsel and co-workers[100−103] have established the importance of step edge decoration as a means for preparing nanowires on a vicinal single-crystal surface using PVD. Control of nanowire "width" and wire spacing has been demonstrated.[103] Long nanowires that are many microns in length have been prepared. In the strongly interacting systems investigated to date, however, the nanowires prepared are a few atomic layers in thickness irrespective of their width. A promising variant of step edge decoration is shadow deposition in which PVD is carried out at gracing incidence on vicinal single-crystal surfaces. Sugawara et al.[104] have recently reported the preparation of arrays of three-dimensional iron nanowires on NaCl(110) using this approach. Electrochemists may have been the first to suggest that step edge decoration occurs in the electrodeposition of metals on vicinal single crystal surfaces. As early as 1988, Clavelier and co-workers[105] interpreted voltammetric peaks observed during the electroplating of bismuth on Pt(332) as selective electrodeposition at steps. Direct confirmation of electrochemical step edge decoration has been provided by STM investigations such as those reported by Behm and co-workers.[106] With regard to electrochemical step decora-
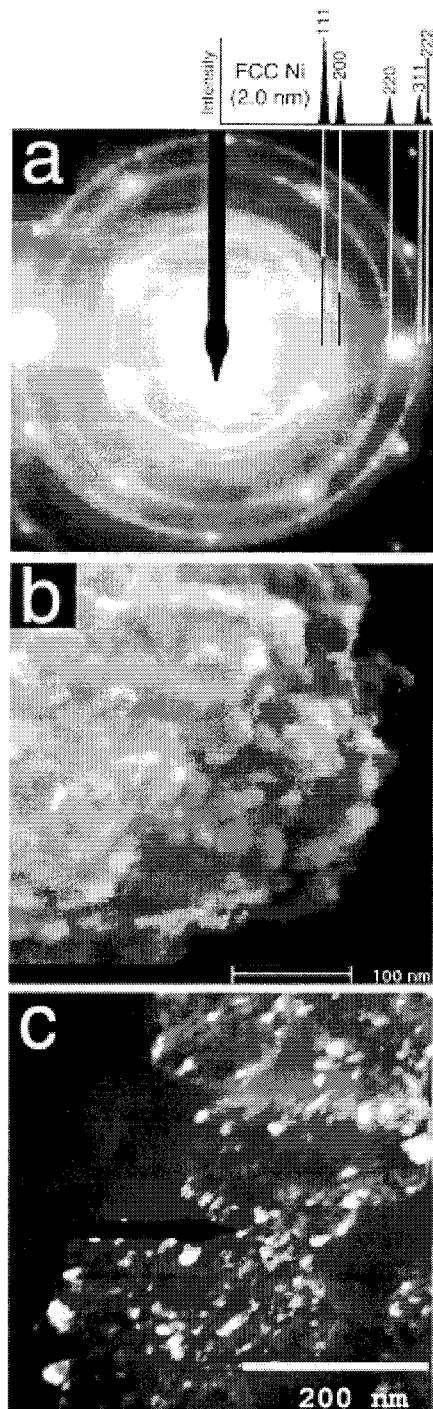
Figure 13. (a) Selected area electron diffraction pattern for the nickel nanoparticles produced using H_2 coevolution method. At top is shown the electron intensity profile expected for FCC nickel nanocrystallites having a diameter of 2 nm. (b) High magnification SEM image of a single, 500 nm diameter nickel particle showing the textured topography. (c) Transmission electron microscope darkfield image of several ~100 nm diameter nickel nanoparticles deposited at −2.0 V for 1.5 s. The 111 diffracted beam was used for imaging.

tion, we make particular note of a recent paper from Myrick and co-workers[107] in which the growth of polypyrrole nanowires on stepped graphite surfaces was described.

We have electrodeposited two types of nanowires in our laboratory to date: noble metal nanowires (e.g., Pd,[108] Cu, Au, and Ag) and nanowires composed of electronically conductive metal oxides (MoO$_2$,[109] Cu$_2$O, and Fe$_2$O$_3$). In this latter case, nanowires composed of molybdenum, copper, and iron have
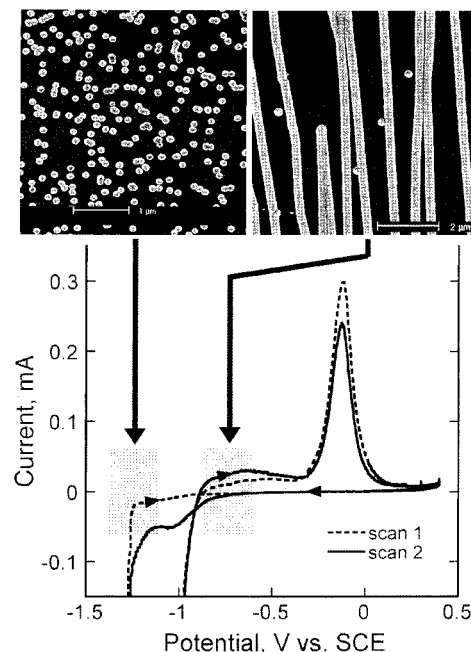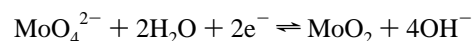

Figure 14. Cyclic voltammograms at 2 mV s^{-1} for a graphite electrode in aqueous 1.0 mM MoO$_4^{2-}$, 1.0 M NaCl, 1.0 M NH$_4$Cl, pH = 8.5. The potential ranges where particle and nanowires are obtained are shown in gray.

been obtained from the parent oxide by gas-phase reduction at elevated temperature cf. ref 109. Here we address the questions, "How can electrodeposition be used to obtain nanowires?" and "What are the advantages of electrodeposition, if any, relative to physical vapor deposition for nanowire growth?"

Our first attempts to prepare nanowires focused on the electrodeposition at graphite surfaces of electronically conductive metal oxides including MoO$_2$, Fe$_2$O$_3$, and Cu$_2$O. Metal oxides were selected in preference to metals because nanowire growth was more easily achieved. Among these metal oxides, MoO$_2$ was studied most intensively. The plating reaction for MoO$_2$ is

$$MoO_4^{2-} + 2H_2O + 2e^- \rightleftharpoons MoO_2 + 4OH^-$$

A cyclic voltammogram for a 2.0 mM solution of MoO$_4^{2-}$ in a pH = 8.5 buffer is shown in Figure 14. This CV is similar to that seen for metals on graphite surfaces (compare with Figures 6a and 10a), and the slow growth method described in section III may also be used to electrodeposit dimensionally uniform particles of MoO$_2$: At a clean graphite surface, the plating potential is first pulsed to −1.2 V vs SCE for a few milliseconds, and the MoO$_2$ nuclei formed are then grown for a much longer time using a potential of −0.7 to −0.9 V vs SCE. As discussed earlier, the purpose of the large amplitude plating pulse is to cause the nucleation of MoO$_2$ nonselectively at both steps and terraces on the graphite surface. Defect-selective electrodeposition of MoO$_2$ at step edges is therefore obtained simply by omitting the nucleation pulse from this sequence. SEM images of typical MoO$_2$ nanowires obtained using this approach are shown in Figure 15.

The defect-selective electrodeposition of MoO$_2$ nanowires occurs at low current densities of 5−40 μA cm^{-2}, and growth times range from a few seconds for 10−20 nm diameter wires to hundreds of seconds for 0.5 μm diameter nanowires. Just as in the slow growth experiment, the deposition current rapidly becomes time independent (±5%) indicating that deposition is
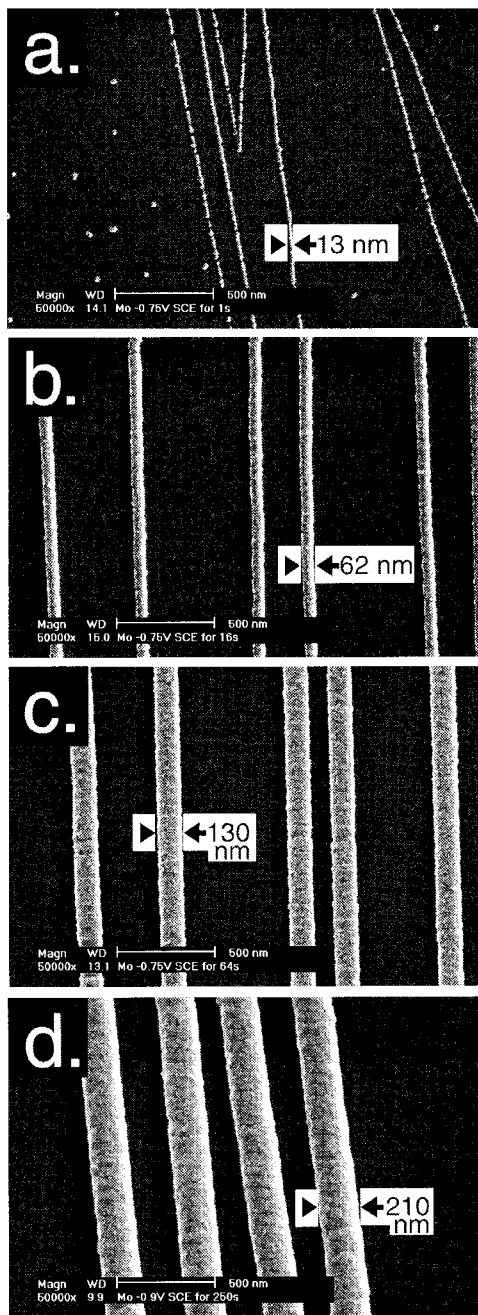
Feature Article

J. Phys. Chem. B, Vol. 106, No. 13, 2002 **3349**

Figure 15. SEMs of graphite surfaces following the electrodeposition of MoO$_2$ nanowires at -0.75 V vs SCE from a plating solution containing 1.0 mM MoO$_4^{2-}$. Nanowires obtained using a deposition duration, (a) $t_{dep} = 1.0$ s; (b) $t_{dep} = 4.0$ s; (c) $t_{dep} = 16.0$ s; (d) $t_{dep} = 256$ s.

convection controlled.[110] Under these conditions, the radii of the nanowires growing on the surface, $r(t)$, is related in a simple way to the deposition time, t_{dep}:[109]

$$r(t) = \sqrt{\frac{2i_{dep}t_{dep}V_m}{\pi n Fl}} \qquad (7)$$

where l is the total length of nanowires on the electrode surface. As shown in Figure 16, the $r(t) \propto t^{1/2}$ functionality predicted by eq 7 is seen experimentally. Thus, eq 7 provides a convenient means for preparing MoO$_2$ nanowires of any diameter with high precision at the outset of a growth experiment. In addition to MoO$_2$, we have obtained nanowires of Fe$_2$O$_3$ and Cu$_2$O using analogous plating conditions. These three metal oxides have in
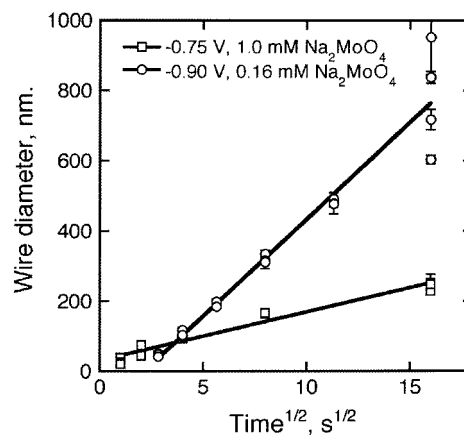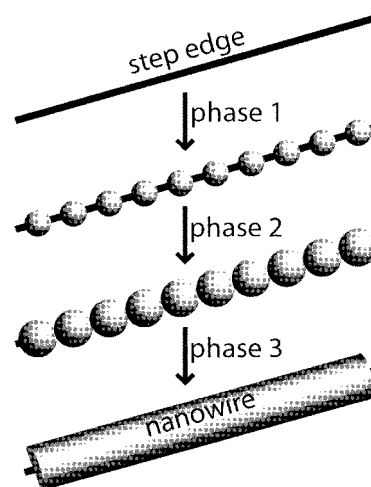

Figure 16. Diameter of MoO$_2$ nanowires versus the square root of the deposition time for two series of depositions as indicated.

SCHEME 4: Three Phases of Nanowire Electrodeposition at Step Edges

common the propensity to nucleate along step edges with a high linear density of >20 μm^{-1}. This means adjacent metal oxide nuclei coalesce rapidly with continued growth yielding continuous nanowires.

Nanowire electrodeposition occurs in three phases as shown in Scheme 4: 1. Metal nuclei form along step edges. 2. Nucleation ceases; hemispherical nuclei grow to coalescence with nearest neighbors forming a rough or "beaded" nanowire. 3. A beaded nanowire grows. As depicted in Scheme 4, phase 3 growth of metal oxide nanowires is characterized by a smoothing of the nanowire surface. For the growth of MoO$_2$ nanowires, for example, the transition from phase 2 to phase 3 growth occurs at a wire diameter of $10-15$ nm. MoO$_2$ nanowires at this juncture have a beaded topology that can be seen in the SEM of Figure 15a. With continued growth to a diameter of 60 nm, smooth hemicylindrical nanowires are obtained as shown in Figure 15b. Nanowire smoothing in phase 3 is probably brought about by the $r \propto t^{1/2}$ functionality of eq 7, as already discussed for metal nanoparticles.

We have started to investigate the diffusional growth of beaded nanowires using Brownian dynamics. In these simulations, the profile of a phase 3 beaded nanowire in the direction parallel to the step edge is approximated by a sine function. The profiles of two such nanowires are shown in Figure 17 parts a and b. Initially, these nanowires have a mean radius of 0.7 nm and a roughness "amplitude" of 1.0 nm. The "wavelength" of the roughness, N_L^{-1}, is the distance between nuclei
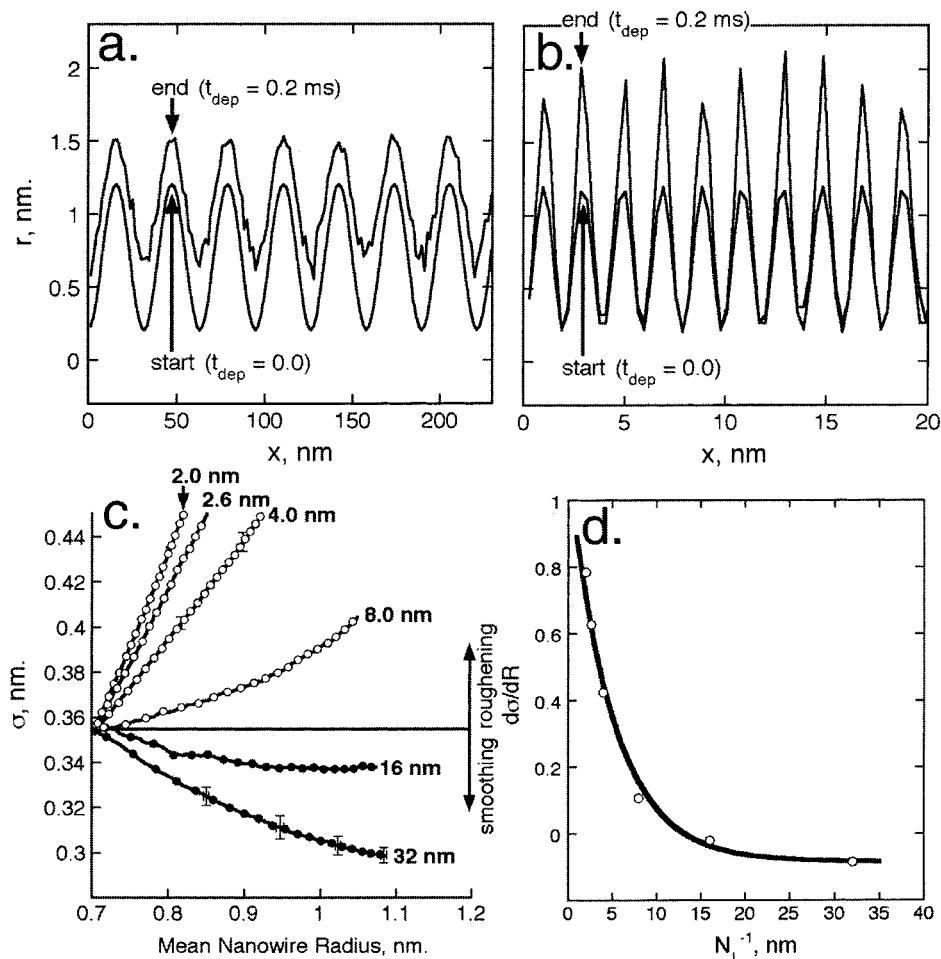
Figure 17. Brownian dynamics simulations of metal nanowire diffusional smoothing and roughening. (a and b) Cross-sections of two nanowires before and following deposition at diffusion control for 0.2 ms. (c) Plots of σ_r versus $\langle r \rangle$ for nanowires during growth at diffusion control. Numbers labeling each plot indicate the period of the sinusoidal "roughenness" of each wire, N_L^{-1}. (d) Plot of $d\sigma_r/dr$ versus N_L^{-1}.

along the step edge or, equivalently, the reciprocal of the linear nucleation density along the step edge, N_L. We have investigated the growth of nanowires with N_L^{-1} values ranging from 30 nm ($N_L \sim 30$ μm^{-1}) down to 2.0 nm. $N_L^{-1} = 30$ nm is the experimental case for MoO$_2$ nucleation on graphite at low overpotentials and, as shown in Figure 17 parts a and c, these nanowires become smoother as a function of growth time. This result is in accordance with our experimental observations and the expectations of eq 7. Although we focus attention on intrananowire smoothing in these simulations, it is naturally the case that narrowing of the diameter distribution for the ensemble of nanowires growing on the surface will also occur under these conditions. Surprisingly, the rate of smoothing, $d\sigma/dr$, decreases as N_L increases as shown in Figure 17 parts c and d. In fact, for internuclei spacings below 16 nm, nanowires become rougher, not smoother, with increasing size during growth. Nanowire roughening for $N_L^{-1} < 16$ nm, seen in Figure 17 parts c and d, is contrary to the predictions of eq 7 and is caused by the inability of ions to diffusionally access the narrow segments of a nanowire. Rapid, dendritic growth of the outermost wire surfaces is, instead, observed as shown in Figure 17b. So far we have not encountered the high nucleation densities associated with roughening in our experiments.

Compared with metal oxides, it is more difficult to obtain metal nanowires by electrodeposition. When metal nanowires are nucleated using low overpotentials of $<|-200$ mV$|$, the nucleation density along steps is <5 μm^{-1}, and micron-scale wires, not nanowires, are obtained. This problem is encountered

with a variety of metals including copper, silver, gold, and palladium. Nanowires of these metals can nevertheless be obtained in parallel with the growth of metal particles on graphite surfaces by altering the technique used for depositing oxide nanowires in two ways. First, a nucleation pulse is applied, and second, a much lower growth rate than that used with metal oxides is employed. This experiment is therefore similar to a slow growth experiment except that a nucleation pulse of lower amplitude is employed to discriminate as much as possible against particle nucleation on terraces while promoting a higher N_L and concomitant nanowire growth on step edges.

In the specific case of palladium, for example, the growth of nanowires involves the application of a -0.2 V vs SCE $\times$ 5 ms pulse followed by growth at $+0.3$ to $+0.4$ V vs SCE. As shown in the cyclic voltammogram of Figure 18a, the pulse potential is 800$-$900 mV negative of the reversible potential for palladium plating. As shown in Figure 18b, the growth rate employed following the nucleation pulse is much lower than for metal oxides, such as MoO$_2$. The combined effect of the nucleation pulse and the slower growth rate is to increase the nucleation density along step edges with the result that continuous Pd nanowires as small as 50 nm can be obtained.

Typical SEM images of palladium nanowires obtained using this approach are shown in Figure 19. A large number of palladium particles are produced in parallel with the Pd nanowires on the terraces adjacent to step edges, and the step-edge selectivity is therefore worse than in the case of nanowire growth experiments involving metal oxides described earlier.
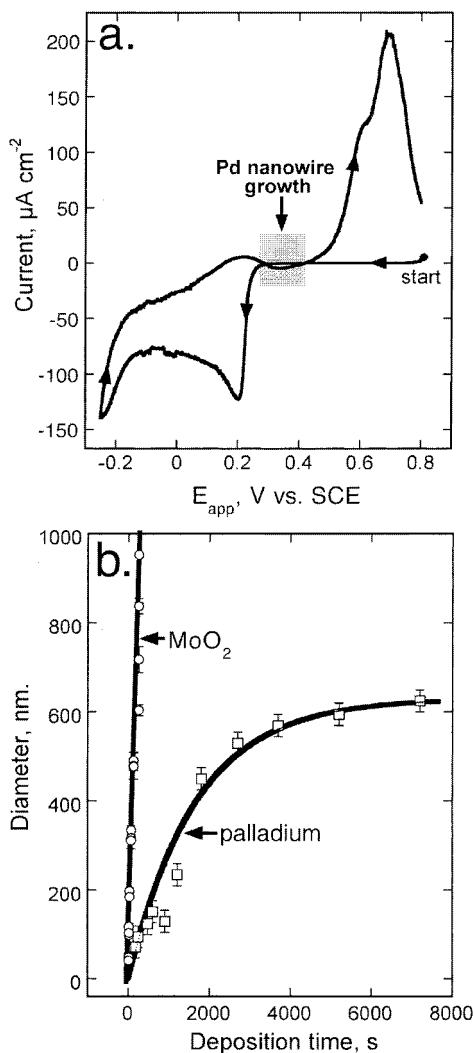
Feature Article

J. Phys. Chem. B, Vol. 106, No. 13, 2002 **3351**

Figure 18. (a) Cyclic voltammogram for a graphite electrode in aqueous 2.0 mM Pd^{2+}, 0.10 M HCl. The potential range used for the growth of Pd mesowires is indicated in gray. (b) Plots of wire diameter versus time for the electrodeposition of MoO_2 nanowires (using the plating solution of Figure 14) and palladium nanowires (from the solution in a).

Figure 19. (a and b) Scanning electron micrographs (SEMs) of Pd mesowires prepared by electrodeposition from aqueous 2.0 mM $PdCl_2$, 0.1 M HCl, $E_{dep} = 0.3$ V, $t_{dep} = 900$ s; (c and d) from aqueous 2.0 mM $Pd(NO_3)_2$, 0.1 M $HClO_4$, $E_{dep} = 0.3$ V, $t_{dep} = 150$ s.

Fortunately, these metal particles are inconsequential for many of the projected applications of these wires (e.g., ref 108). We have recently demonstrated the operation of hydrogen sensors and hydrogen-actuated switches based on arrays of palladium nanowires that are embedded in plastic and lifted off of graphite surfaces.[108]

Summary

Electrodeposition on graphite is a surprisingly versatile way to prepare metal particles and nanowires that are dimensionally uniform and, in the case of nanowires, extremely long. Brownian dynamics simulations coupled with experimental studies have yielded a satisfactory, "first order" understanding of the factors affecting size dispersion in nanostructure electrodeposition (predominantly IDC). This understanding has led to the development of the slow growth and H_2 coevolution methods described in this paper. Our experimental data suggests that other processes that we have not yet identified may contribute to size dispersion. One example is the following: silver particle size distributions such as those shown in Figure 8b to not become narrower with growth time in accordance with eq 7. These processes must be identified and controlled before the size
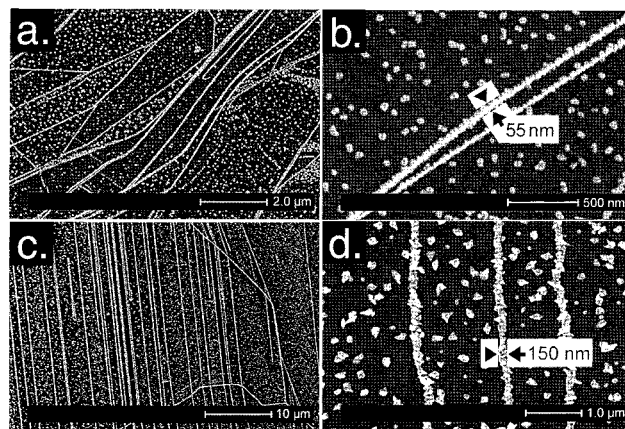
dispersion achievable for metal particles in the 10−100 nm diameter range can compete with state-of-the art colloid synthesis methods. With regard to metal nanowires, the combination of nanoscopic wire diameter, uniformity, and length available using step edge decoration on graphite is already very good. However it remains impossible to prepare noble metal nanowires narrower than 50 nm. Further progress in this direction will require new methods for increasing the linear nucleation density selectively along steps without promoting nucleation on terraces.

Especially in view of the restricted scope of this article with regard to the electrode material, it is important to note that highly oriented pyrolytic graphite possesses a unique combination of properties that lend it to this application. These properties are the following: (1) low resistivity (10^{-3} Ω cm), (2) low surface free energy (35 dyne cm^{-1} [111]) which is responsible for the Volmer−Weber growth mode seen for all metals on the graphite basal plane, (3) excellent chemical inertness, which ensures that deposited mesostructures interact primarily via van der Waals interactions and can therefore be easily removed (the disadvantage that the graphite surface is technologically irrelevant is partially mitigated by the ease with which nanostructures can be lifted off it), (4) large grain size up to millimeters, and the property that within a single grain, step edges are linear and oriented, and finally, (5) extremely anisotropic electrochemical properties (defect-free terraces are electrochemically inert or nearly so; step edges behave like linear microelectrodes).[112−115] We have expended considerable effort to extend nanostructure growth to hydrogen passivated silicon surfaces; however, the same degree of size selectivity has not been obtainable in these studies.

Scholar award. Finally, the work described here would have been much more expensive without the generosity of Dr. Art Moore of Advanced Ceramics who has provided my group with graphite for 10 years.

References and Notes

(1) Mesoscopic structures are characterized by a length scale ranging from 10 nm to microns.

(2) Ahmadi, T. S.; Wang, Z. L.; Green, T. C.; Henglein, A.; Elsayed, M. A. *Science* **1996**, *272*, 1924.

(3) Ahmadi, T. S.; Wang, Z. L.; Henglein, A.; El-Sayed, M. A. *Chem. Mater.* **1996**, *8*, 1161.

(4) Ducamp-Sanguesa, C.; Herrera-Urbina, R.; Figlarz, M. *J. Solid State Chem.* **1992**, *100*, 272.

(5) Ershov, B. G.; Henglein, A. *J. Phys. Chem. B* **1998**, *102*, 10663.

(6) Frens, G. *Nature* **1973**, *241*, 20.

(7) Gutierrez, M.; Henglein, A. *J. Phys. Chem.* **1993**, *97*, 11368.

(8) Henglein, A. *Chem. Rev.* **1989**, *89*, 1861.

(9) Henglein, A. *J. Phys. Chem. B* **2000**, *104*, 1206.

(10) Henglein, A.; Giersig, M. *J. Phys. Chem. B* **1999**, *103*, 9533.

(11) Henglein, A.; Linnert, T.; Mulvaney, P. *Ber. Buns. Ges. Phys.* **1990**, *94*, 1449.

(12) Henglein, A.; Meisel, D. *Langmuir* **1998**, *14*, 7392.

(13) Huang, Z. Y.; Mills, G.; Hajak, B. *J. Phys. Chem.* **1993**, *97*, 11542.

(14) Jao, T.-C.; Beddard, G. S.; Tundo, P.; Fendler, J. H. *J. Phys. Chem.* **1981**, *85*, 1963.

(15) Leff, D. V.; Ohara, P. C.; Heath, J. R.; Gelbart, W. M. *J. Phys. Chem.* **1995**, *99*, 7036.

(16) Longenberger, L.; Mills, G. *J. Phys. Chem.* **1995**, *99*, 475.

(17) Mohamed, M. B.; Wang, Z. L.; El-Sayed, M. A. *J. Phys. Chem. A* **1999**, *103*, 10255.

(18) Overbeek, J. T. G. *Adv. Colloid Interface Sci.* **1982**, *15*, 251.

(19) Puntes, V. F.; Krishnan, K. M.; Alivisatos, A. P. *Science* **2001**, *291*, 2115.

(20) Reetz, M. T.; Helbig, W. *J. Am. Chem. Soc.* **1994**, *116*, 7401.

(21) Sugimoto, T. *Adv. Colloid Interface Sci.* **1987**, *28*, 65.

(22) Sun, S. H.; Murray, C. B. *J. Appl. Phys.* **1999**, *85*, 4325.

(23) Sun, S. H.; Murray, C. B.; Weller, D.; Folks, L.; Moser, A. *Science* **2000**, *287*, 1989.

(24) Teranishi, T.; Hosoe, M.; Miyake, M. *Adv. Mater.* **1997**, *9*, 65.

(25) Jana, N. R.; Gearheart, L.; Murphy, C. J. *J. Phys. Chem. B* **2001**, *105*, 4065.

(26) Jana, N. R.; Gearheart, L.; Murphy, C. J. *Chem. Commun.* **2001**, 617.

(27) Wang, Z. L.; Mohamed, M. B.; Link, S.; El-Sayed, M. A. *Surface Sci.* **1999**, *440*, L809.

(28) RSD$_{dia}$ is the relative standard deviation of the particle diameter: RSD$_{dia} = \sigma/\langle dia \rangle$

(29) LaMer, V. K.; Dinegar, R. H. *J. Am. Chem. Soc.* **1950**, *72*, 4847.

(30) Zoval, J. V.; Lee, J.; Gorer, S.; Penner, R. M. *J. Phys. Chem.* **1998**, *102*, 1166.

(31) Zoval, J. V.; Stiger, R. M.; Biernacki, P. R.; Penner, R. M. *J. Phys. Chem.* **1996**, *100*, 837.

(32) Almawlawi, D.; Liu, C. Z.; Moskovits, M. *J. Mater. Res.* **1994**, *9*, 1014.

(33) Cepak, V. M.; Martin, C. R. *J. Phys. Chem. B* **1998**, *102*, 9985.

(34) Davydov, D. N.; Haruyama, J.; Routkevitch, D.; Statt, B. W.; Ellis, D.; Moskovits, M.; Xu, J. M. *Phys. Rev. B: Condens. Matter* **1998**, *57*, 13550.

(35) Davydov, D. N.; Sattari, P. A.; AlMawlawi, D.; Osika, A.; Haslett, T. L.; Moskovits, M. *J. Appl. Phys.* **1999**, *86*, 3983.

(36) Foss, C. A.; Tierney, M. J.; Martin, C. R. *J. Phys. Chem.* **1992**, *96*, 9001.

(37) Foss, C. A.; Hornyak, G. L.; Stockert, J. A.; Martin, C. R. *J. Phys. Chem.* **1994**, *98*, 2963.

(38) Genzel, L.; Martin, T. P.; Kreibig, U. *Z. Phys. B* **1975**, *21*, 339.

(39) Hong, K. M.; Yang, F. Y.; Liu, K.; Reich, D. H.; Searson, P. C.; Chien, C. L.; Balakirev, F. F.; Boebinger, G. S. *J. Appl. Phys.* **1999**, *85*, 6184.

(40) Hulteen, J. C.; Martin, C. R. *J. Mater. Chem.* **1997**, *7*, 1075.

(41) Liu, H. I.; Maluf, N. I.; Pease, R. F. W.; Biegelsen, D. K.; Johnson, N. M.; Ponce, F. A. *J. Vac. Sci. Technol. B* **1992**, *10*, 2846.

(42) Liu, K.; Nagodawithana, K.; Searson, P. C.; Chien, C. L. *Phys. Rev. B: Condens. Matter* **1995**, *51*, 7381.

(43) Liu, K.; Chien, C. L.; Searson, P. C. *Phys. Rev. B: Condens. Matter* **1998**, *58*, R14681.

(44) Liu, K. I.; Chien, C. L.; Searson, P. C.; YuZhang, K. *Appl. Phys. Lett.* **1998**, *73*, 2222.

(45) Liu, K.; Chien, C. L.; Searson, P. C.; Kui, Y. Z. *IEEE Trans. Magn.* **1998**, *34*, 1093.

(46) Martin, C. R. *Science* **1994**, *266*, 1961.

(47) Martin, C. R. *Chem. Mater.* **1996**, *8*, 1739.

(48) Oskam, G.; Long, J. G.; Natarajan, A.; Searson, P. C. *J. Phys. E: Appl. Phys.* **1998**, *31*, 1927.

(49) Preston, C. K.; Moskovits, M. *J. Phys. Chem.* **1993**, *97*, 8495.

(50) Routkevitch, D.; Tager, A. A.; Haruyama, J.; Almawlawi, D.; Moskovits, M.; Xu, J. M. *IEEE Trans. Electron Devices* **1996**, *43*, 1646.

(51) Sapp, S. A.; Mitchell, D. T.; Martin, C. R. *Chem. Mater.* **1999**, *11*, 1183.

(52) Sun, L.; Searson, P. C.; Chien, C. L. *Appl. Phys. Lett.* **1999**, *74*, 2803.

(53) Tager, A. A.; Xu, J. M.; Moskovits, M. *Phys. Rev. B: Condens. Matter* **1997**, *55*, 4530.

(54) Strbac, S.; Maroun, F.; Magnussen, O. M.; Behm, R. J. *J. Electroanal. Chem.* **2001**, *500*, 479.

(55) Strbac, S.; Magnussen, O. M.; Behm, R. J. *Phys. Rev. Lett.* **1999**, *83*, 3246.

(56) Moller, F. A.; Magnussen, O. M.; Behm, R. J. *Phys. Rev. Lett.* **1996**, *77*, 5249.

(57) Moller, F. A.; Magnussen, O. M.; Behm, R. J. *Phys. Rev. Lett.* **1996**, *77*, 3165.

(58) Kolb, D. M.; Engelmann, G. E.; Ziegler, J. C. *Solid State Ionics* **2000**, *131*, 69.

(59) Kolb, D. M.; Engelmann, G. E.; Ziegler, J. C. *Angew. Chem. Int. Ed.* **2000**, *39*, 1123.

(60) Ziegler, J. C.; Engelmann, G. E.; Kolb, D. M. *Z. Phys. Chem.* **1999**, *208*, 151.

(61) Engelman, G. E.; Ziegler, J. C.; Kolb, D. M. *J. Electrochem. Soc.* **1998**, *145*, 2970.

(62) Kolb, D. M.; Ullmann, R.; Ziegler, J. C. *Electrochim. Acta* **1998**, *43*, 2751.

(63) Engelmann, G. E.; Ziegler, J. C.; Kolb, D. M. *J. Electrochem. Soc.* **1998**, *145*, L33.

(64) Kolb, D. M.; Ullmann, R.; Will, T. *Science* **1997**, *275*, 1097.

(65) Schindler, W.; Koop, T.; Hofmann, D.; Kirschner, J. *IEEE Trans. Magn.* **1998**, *34*, 963.

(66) Schindler, W.; Schneider, O.; Kirschner, J. *J. Appl. Phys.* **1997**, *81*, 3915.

(67) Osaka, T. *Electrochim. Acta* **2000**, *45*, 3311.

(68) Cavallotti, P. L.; Lecis, N.; Fauser, H.; Zielonka, A.; Celis, J. P.; Wouters, G.; daSilva, J. M.; Oliveira, J. M. B.; Sa, M. A. *Surf. Coat. Tech.* **1998**, *105*, 232.

(69) Chassaing, E.; Nallet, P.; Trichet, M. F. *J. Electrochem. Soc.* **1996**, *143*, L98.

(70) Harris, T. M.; Whitney, G. M.; Croll, I. M. *J. Electrochem. Soc.* **1995**, *142*, 1031.

(71) Liao, S. H. *IEEE Trans. Magn.* **1990**, *26*, 328.

(72) *The Fundamentals of Metal Deposition*; Harrison, J. A.; Thirsk, H. R.; Eds.; Marcel Dekker: New York, 1971; Vol. 5.

(73) Stiger, R.; Craft, B.; Penner, R. M. *Langmuir* **1999**, *15*, 790.

(74) Reiss, H. *J. Chem. Phys.* **1954**, *19*, 482.

(75) This equation assumes the solubility of the particle in the growth solution is negligible.

(76) Zangwill, A. *Physics at Surfaces*; Cambridge University Press: Cambridge, U.K., 1988.

(77) Volmer, M.; Weber, A. *Z. Phys. Chem.* **1926**, *119*, 277.

(78) Hsiao, G.; Anderson, M. G.; Gorer, S.; Harris, D.; Penner, R. M. *J. Am. Chem. Soc.* **1997**, *119*, 1439.

(79) Anderson, M.; Gorer, S.; Penner, R. M. *J. Phys. Chem.* **1997**, *101*, 5895.

(80) Gorer, S.; Ganske, J.; Hemminger, J. C.; Penner, R. M. *J. Am. Chem. Soc.* **1998**, *120*, 9584.

(81) Nyffenegger, R. M.; Craft, B.; Shaaban, M.; Gorer, S.; Penner, R. M. *Chem. Mater.* **1998**, *10*, 1120.

(82) Fransaer, J.; Penner, R. M. *J. Phys. Chem. B* **1999**, *103*, 7643.

(83) Penner, R. M. *J. Phys. Chem. B* **2001**, *105*, 8672.

(84) Bobbert, P. A.; Wind, M. M.; Vlieger, J. *Physica A* **1987**, *146*, 69.

(85) Bard, A. J.; Faulkner, L. R. *Electrochemical Methods: Fundamentals and Applications*, 2nd ed.; John Wiley and Sons: New York, 2001.

(86) Gorer, S.; Liu, H.; Stiger, R. M.; Zach, M. P.; Zoval, J. V.; Penner, R. M. Electrodeposition of Metal Nanoparticles on Graphite and Silicon. In *Handbook of Metal Nanoparticles*; Feldheim, D.; Foss, C.; Eds.; Marcel-Dekker: New York, 2001.

(87) Liu, H.; Favier, F.; Ng, K.; Zach, M. P.; Penner, R. M. *Electrochim. Acta* **2001**, *47*, 671.

(88) Liu, H.; Penner, R. M. *J. Phys. Chem. B* **2000**, *104*, 9131.

(89) Sandmann, G.; Dietz, H.; Plieth, W. *J. Electroanal. Chem.* **2000**, *491*, 78.

(90) Plieth, W.; Dietz, H.; Sandmann, G.; Meixner, A.; Weber, M.; Moyer, P.; Schmidt, J. *Electrochim. Acta* **1999**, *44*, 3659.

(91) Bradford, E. B.; Vanderhoff, J. W.; Alfrey, T. J. *J. Colloid Sci.* **1956**, *11*, 135.

(92) Foerster, F. *Trans. Electrochem. Soc.* **1924**, *46*, 23.

(93) Dees, D. W.; Tobias, C. W. *J. Electrochem. Soc.* **1987**, *134*, 1702.

Feature Article

J. Phys. Chem. B, Vol. 106, No. 13, 2002 **3353**

(94) Sutija, D. P.; Tobias, C. W. *J. Electrochem. Soc.* **1994**, *141*, 2599.

(95) (MSE) refers to a mercurous sulfate reference electrode. The MSE has a potential of +0.640 V vs a normal hydrogen electrode (NHE).

(96) Zach, M. P.; Penner, R. M. *Adv. Mater.* **2000**, *12*, 878.

(97) The Scherrer formula is $B = 0.9\lambda/(\tau \cos \theta)$, where B is the width (full width at half-maximum) of the diffraction line (radians), λ is the deBroglie wavelength of the electron (Å), τ is the diameter of the crystallite (Å), and θ the angle subtended by the beam and the diffracting plane.

(98) Martin, B. R.; Dermody, D. J.; Reiss, B. D.; Fang, M. M.; Lyon, L. A.; Natan, M. J.; Mallouk, T. E. *Adv. Mater.* **1999**, *11*, 1021.

(99) Zhang, Y.; Franklin, N. W.; Chen, R. J.; Dai, H. J. *Chem. Phys. Lett.* **2000**, *331*, 35.

(100) Himpsel, F. J.; Jung, T.; Ortega, J. E. *Surf. Rev. Lett.* **1997**, *4*, 371.

(101) Himpsel, F. J.; Jung, T.; Kirakosian, A.; Lin, J. L.; Petrovykh, D. Y.; Rauscher, H.; Viernow, J. *MRS Bull.* **1999**, *24*, 20.

(102) Jung, T.; Schlittler, R.; Gimzewski, J. K.; Himpsel, F. J. *Appl. Phys. A: Mater. Sci. Process* **1995**, *61*, 467.

(103) Petrovykh, D. Y.; Himpsel, F. J.; Jung, T. *Surf. Sci.* **1998**, *407*, 189.

(104) Sugawara, A.; Coyle, T.; Hembree, G. G.; Scheinfein, M. R. *Appl. Phys. Lett.* **1997**, *70*, 1043.

(105) Clavilier, J.; Feliu, J. M.; Aldaz, A. *J. Electroanal. Chem.* **1988**, *243*, 419.

(106) Nichols, R. J.; Kolb, D. M.; Behm, R. J. *J. Electroanal. Chem.* **1991**, *313*, 109.

(107) Noll, J. D.; Nicholson, M. A.; VanPatten, P. G.; Chung, C. W.; Myrick, M. L. *J. Electrochem. Soc.* **1998**, *145*, 3320.

(108) Favier, F.; Walter, E.; Zach, M. P.; Benter, T.; Penner, R. M. *Science* **2001**, *293*, 2227.

(109) Zach, M. P.; Ng, K. H.; Penner, R. M. *Science* **2000**, *290*, 2120.

(110) This plating solution is unstirred. The convection that is present in the electrochemical cell is brought about by temperature and density gradients.

(111) Morcos, I. *J. Chem. Phys.* **1972**, *57*, 1801.

(112) Bowling, R. J.; Packard, R. T.; McCreery, R. L. *J. Am. Chem. Soc.* **1991**, *111*, 1217.

(113) Cline, K. K.; McDermott, M. T.; McCreery, R. L. *J. Phys. Chem.* **1994**, *98*, 5314.

(114) Robinson, R. S.; Sternitzke, K.; McDermott, M. T.; McCreery, R. L. *J. Electrochem. Soc.* **1991**, *138*, 2412.

(115) Bowling, R. J.; McCreery, R. L.; Pharr, C. M.; Engstrom, R. C. *Anal. Chem.* **1989**, *61*, 2763.